Available online at www.sciencedirect.com
SCIENCE DIRECT®
Computational Materials Science 34 (2005) 299–313
COMPUTATIONAL MATERIALS SCIENCE
www.elsevier.com/locate/commatsci

2D cellular automaton simulation of the recrystallization texture of an IF sheet steel under consideration of Zener pinning

Dierk Raabe [a,*], Luc Hantcherli [b]

[a] Max-Planck-Institut für Eisenforschung, Max-Planck-Strasse 1, 40237 Düsseldorf, Germany
[b] Ecole National Superieur des Mines de Saint-Etienne, 158 Cours Fauriel, 42023 Saint Etienne Cedex 2, France

Received 11 October 2004; received in revised form 25 November 2004; accepted 17 December 2004

Abstract

This is a 2D cellular automaton simulation study on the evolution of the recrystallization texture in a 75% cold rolled interstitial free (IF) sheet steel. The model is applied to experimentally obtained high resolution microtexture EBSD data. The simulation is discrete in time and physical space. Orientation is treated as a continuous variable in Euler space. The dislocation density distribution is approximated from the Kikuchi pattern quality of the experimental EBSD data. It is used for the calculation of the scalar driving force field required for the recrystallization simulation. Different models for nucleation and for the influence of Zener-type particle pinning are presented and tested. Real time and space calibration of the simulation is obtained by using experimental input data for the grain boundary mobility, the driving forces, and the length scale of the deformed microstructure as mapped by the high resolution EBSD experiments. The simulations predict the kinetics and the evolution of microstructure and texture during recrystallization. Depending on the ratio of the precipitated volume fraction and the average radius of the particles the simulations reveal three different regimes for the influence of particle pinning on the resulting microstructures, kinetics and crystallographic textures.

Keywords: Texture; Microtexture; Stored energy; Automotive; EBSD; Nucleation; Grain growth

1. Introduction

The understanding of the recrystallization texture of interstitial free (IF) low carbon steel sheets is important for an improved prediction of the resulting elastic-plastic anisotropy of such steels with respect to their engineering performance

* Corresponding author. Tel.: +49 211 6792278; fax: +49 211 6792333.
E-mail address: raabe@mpie.de (D. Raabe).

0927-0256/$ - see front matter © 2005 Elsevier B.V. All rights reserved.
doi:10.1016/j.commatsci.2004.12.067

during sheet forming in the automotive industry. The main goal in that context is to produce IF steel sheets with a very strong and homogeneous γ-fiber texture ($\{1\,1\,1\}\langle uvw\rangle$ texture) and a very small orientation density of the 45° ND-rotated cube orientation, $\{0\,0\,1\}\langle 1\,1\,0\rangle$ (ND refers to the sheet normal direction). The beneficial mechanical properties resulting from such textures, namely, a maximum planar Lankfort value together with a minimum variation of the Lankfort value in the sheet plane, define the goal for optimizing corresponding industry-scale continuous annealing procedures for IF steels for better sheet drawability [1–9].

An important microstructural parameter affecting the formation of recrystallization textures in IF steels is the influence of incoherent second phase precipitates which are located on the inherited grain boundaries of the deformed grains (e.g., aluminium-nitrides, titanium-carbides, titanium-sulfides, titanium-carbonitrides). In this study we use a modified 2D cellular automaton approach [10] for the simulation of primary static recrystallization of a cold rolled IF sheet steel (75% engineering thickness reduction). The proposed modification of the automaton consists in the possibility to consider the pinning effect associated with particles at the former grain boundaries according to the Zener or respectively Zener–Friedel models [11]. The automaton is used in a 2D rather than in the standard 3D formulation [10] since in the current study it is applied to experimental 2D EBSD data of the starting microstructure. The motivation for this simulation study is the frequent observation that new grains which grow during primary static recrystallization in such steels do not easily expand across the former grain boundaries of the deformed microstructure [9,12].

Our own TEM-observations have revealed the presence of fine particles (in particular of Ti(C,N)) at the inherited grain boundaries surrounding the deformed grains, so that one possible explanation for the impeded recrystallization may be a strong particle pinning effect (Fig. 1). The goal of this study, hence, is to investigate the influence of such fine grain boundary particles on the recrystallization microstructure and texture with the help of a modified cellular automaton approach.

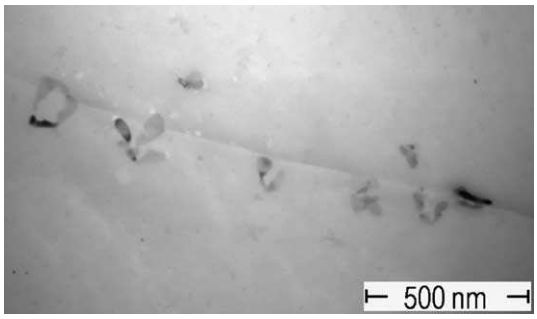

Fig. 1. TEM-carbon-replica of Ti(CN) precipitations on a grain boundary in an IF steel before recrystallization [unpublished results by I. Thomas, MPI].

2. Cellular automaton model

2.1. Basics of cellular automata for recrystallization modeling

Cellular automata are algorithms that describe the discrete spatial and temporal evolution of complex systems by applying local deterministic or probabilistic transformation rules to the cells of a regular (or non-regular) lattice [13–17]. These rules determine the state of a lattice point as a function of its previous state and the state of the neighboring sites. The number, arrangement, and range of the neighbor sites used by the transformation rule for calculating a state switch determines the range of the interaction and the local shape of the areas which evolve. Cellular automata work in discrete time steps. After each time interval the values of the state variables are updated for all lattice points in synchrony mapping the new (or unchanged) values assigned to them through the local transformation rule. Owing to these features, cellular automata provide a discrete method of simulating the evolution of complex dynamical systems which contain large numbers of similar components on the basis of their local interactions. The overall spatial system complexity and transformation kinetics emerge from the repeated and synchronous application of the cellular automaton rules equally to all nodes of the lattice. These local rules can for many cellular automaton models in materials science be derived through finite difference formulations of the underlying differential equa-

tions that govern the system dynamics at a mesoscopic level [15,16]. Cellular automata have been successfully used for a variety of problems in the field of recrystallization [15–30]. The model for the present recrystallization simulation is designed as a cellular automaton with a probabilistic transformation rule. The details of the used transformation rules are given in [10,16,26].

2.2. Particle pinning forces on grain boundaries

Grain boundary pinning forces arise when second phase particles occur on the grain boundary. Their presence reduces the grain boundary area and, hence, the grain boundary energy. This energy saving which must be replenished upon unpinning is referred to as Zener pinning [11,31]. In the following simulations we consider pinning effects imposed by a stable array of incoherent particles which reside on the grain boundaries of the deformed microstructure.

In his first calculation Zener [11] approximated the magnitude of the pinning force by assuming randomly distributed spherical particles. The boundary was assumed to move as a straight interface through the particle array and to experience a resistive force, F, from each particle. With γ the boundary energy (in units of J/m^2), the force F due to one particle is given by $F = \pi r\gamma$, where r is the particle radius. The surface A on which the force is applied amounts to $A = 2\pi r^2/(3f)$, where f is the volume fraction of spherical particles. The Zener pressure then amounts to

$$p_{\mathrm{Z}} = -\frac{3}{2}\gamma\frac{f}{r} \tag{1}$$

A shortcoming of this approach is that a grain boundary cannot be considered as a rigid interface, but it may have some flexible to bow out between particles when a driving force is applied. Diverse modifications have been proposed to correct for this flexibility [31–33]. They give results which are of the same order of magnitude as the original formulation of Zener. Two possible corrections were discussed by Hunderi and co-workers [34,35], p_{HZ}. They introduce a correction factor Φ which depends on the volume fraction of the particles f:

$$p_{\mathrm{HZ}} = -\Phi(f)\frac{3}{4}\gamma\frac{f}{r} \tag{2}$$

When assuming a Friedel-like particle behavior one obtains the following equation for the drag force, p_{FZ},

$$p_{\mathrm{FZ}} = -2.6\gamma\frac{f^{0.92}}{r} \tag{3}$$

When considering a stronger dependence of the corrector factor on the value of f than assumed in the original Friedel model [34–36], one obtains a modified expression for the Zener pressure:

$$p_{\mathrm{LFZ}} = -0.33\gamma\frac{f^{0.87}}{r} \quad \text{for } f < 3\% \tag{4}$$

For a reasonable choice of the grain boundary energy (0.6 J/m^2), the precipitate volume fraction (1%), and the average particle radius (1000 Å) the original Zener pinning force, as calculated according to Eq. (1) amounts to about 0.1 MPa. When considering the corrections discussed, the pinning force rises to about 0.5 MPa according to Eq. (3) and to 0.2 MPa according to Eq. (4). Eqs. (1) and (3) are hereafter used as constitutive laws for the simulations.

2.3. Implementation of Zener-type pinning effects into the cellular automaton

The introduction of a Zener-like pinning effect according to Eqs. (1) and (3) requires the definition of three new state variables in the recrystallization cellular automaton algorithm, namely, the grain boundary energy per area, the volume fraction of incoherent second phase particles, and the average particle size. The actual implementation of these quantities and the calculation of the resulting forces in a cellular automaton approach depends strongly on how the particles are modeled in the algorithm. Two different methods are conceivable to map particles on the inherited grain boundaries in a cellular automaton.

The first model defines a fixed volume fraction of particles as an attribute to each *cell* abutting an existing grain boundary. Since particles which are relevant for pinning effects are small compared to the cell size of the automaton they cannot be mapped in a one-to-one fashion occupying a

complete cell. A specific volume fraction of particles (and also a local value for the particle size) is, instead, associated with each cell abutting a grain boundary. This description has the advantage that it can smoothly enter into the standard automaton algorithm. The concept also allows one to start with a heterogeneous distribution of particles on the grain boundaries. The second model defines the volume fraction of particles as a generic grain boundary parameter and not as a cell variable. This means that the particle volume fraction and average radius is defined together with the type of grain boundary. In the following we use the second approach to map particles in the automaton mesh.

2.4. Criterion for recrystallization nucleation events

Primary static recrystallization proceeds by the formation and growth of nuclei [31]. In the present model the nucleation stage is not explicitly simulated since the automaton works above the subgrain scale. This means that the current automaton model with its rather large cell size cannot explicitly be used to model discontinuous subgrain coarsening phenomena which entail nucleation in IF steels. The transformation rule of the cellular automaton explained above considers only the growth stage. This means that a nucleation criterion must be added as a separate model. Such a nucleation rule determines how the incipient stage of recrystallization is seeded. A nucleation rule has to fulfill the kinetic and thermodynamic instability criteria. The kinetic instability criterion means that a successful nucleation event leads to the formation of a mobile large angle grain boundary (misorientation above 15°) that can sweep the surrounding deformed matrix. The thermodynamic instability criterion means that the stored energy changes across the newly formed large angle grain boundary creating a driving force that pushes it forward into the surrounding deformed matrix. The latter step is captured by the transformation rule of the cellular automaton as outlined above.

The nucleation rule chosen in this simulation study is based on site saturated nucleation conditions. At the beginning of the algorithm, the local values of the stored deformation energy (dislocation density) are for each cell checked and compared to some critical value. If the local value of the dislocation density is larger than that critical value, the cell is considered as spontaneously recrystallized without any orientation change [16,17]. In practice, this means for a cell that its orientation attributes (Euler angles) remain unchanged whereas the stored energy density parameter (dislocation density) drops to zero. With this step, the thermodynamic criterion is fulfilled. In the ensuing time step a so recrystallized cell can attempt to sweep a non-recrystallized neighbor cell according to the transformation rule, i.e., it is only successful if one of its boundary segments has sufficient mobility and a sufficiently large net driving force to move.

2.5. Grain boundary input parameters for the simulations

The IF steel investigated is characterized by 1810 K for the melting point; 2.480 Å for the Burgers vector at 300 K; $15 \times 10^{-6}\,\mathrm{K}^{-1}$ for the thermal dilatation coefficient; 69.2 GPa for the shear modulus at 300 K; 0.015 GPa/K for the thermal stiffness dilatation coefficient of the shear modulus; and a Poisson coefficient of 0.3. The grain boundary mobility data used for large angle interfaces in the current simulations are taken from experiments on Fe–Si specimens [37–39], namely, $97.48 \times 10^{-2}\,\mathrm{m}^3/\mathrm{N\,s}$ for the pre-exponential factor of the mobility and 3.9 eV for the energy of activation of the grain boundary mobility. These values are applied for large angle grain boundaries irrespective of their boundary plane normal. The dependence of the grain boundary mobility on the orientation difference of the neighboring grains as used in this study is given by

$$m(\theta) = \left[0.9\left(\frac{1}{1+\exp[(-2)\times(\theta-15)]}\right)\right] + 1 \quad (5)$$

For the grain boundary energy and its dependence on the misorientation angle we use the Read-Shockley approximation for angles below 15° [31]

$$\gamma = \gamma_{\mathrm{HAGB}}\frac{\theta}{\theta_{\mathrm{HAGB}}}\left(1 - \ln\left(\frac{\theta}{\theta_{\mathrm{HAGB}}}\right)\right) \quad (6)$$

where γ_{HAGB} is the high angle grain boundary specific energy, θ the misorientation angle and θ_{HAGB} is the transition limit to the high angle grain boundary regime which is described by a grain boundary energy of 0.79 J/m^2.

2.6. Stored energy input data for the simulations

Several authors have suggested approaches to estimate the stored deformation energy in rolled steel sheets from EBSD data. Choi et al. [40,41] have recently discussed three different methods. The first one uses the Kikuchi pattern quality of the EBSD data. The authors suggest, that this parameter can be related to the dislocations density. They assume that a high magnitude of the image quality corresponds to a small value of the stored deformation energy. The authors suggest that the stored energy for each cell, E_i, can be expressed as being proportional to the image quality distribution for each measured point, I_i, according to the relation

$$E_i \propto I_i = 10\left(1 - \frac{Q_i - Q_{min}}{Q_{max} - Q_{min}}\right) \tag{7}$$

where Q_i is the image quality at the measured point I, and Q_{max} and Q_{min} are the maximum and minimum values of the image quality at that point, respectively. The factor is chosen to obtain values between 0 and 10 MPa for the driving force. The dislocation density for each cell ρ_i can then be evaluated by using

$$\rho_i \propto \frac{2I_i}{Gb^2} = \frac{2\times 10^7}{Gb^2}\left(1 - \frac{Q_i - Q_{min}}{Q_{max} - Q_{min}}\right) \tag{8}$$

where G is the shear modulus and b the Burgers vector. It is obvious though that this method is affected by experimental details such as specimen preparation and contamination effects.

The second method described in [40,41] uses the Taylor model. In this approach it is suggested that the stored deformation energy of each cell can be related to the Taylor factor, M_i, which is the sum of crystallographic shear for an imposed von Mises strain step. The authors discuss that cells which have a small Taylor factor correspond to areas with a high deformation potential, and thus to areas with a high stored deformation energy. In our view this evaluation method has two drawbacks: First, the method cannot properly capture the inhomogeneity of the deformation [42]. Second, the Taylor factor alone only gives an image of the current deformation state and does not consider the deformation history. It is clear, however, that the accumulation of the stored energy during a deformation path is determined not only by the *final* Taylor factor but by the path that the Taylor factor takes during grain rotation in the course of deformation.

The third method discussed by the authors [40,41] is based on the subgrain substructure. When assuming that the dislocation substructure can be simplified in form of circular subgrains of radius r and a subgrain boundary energy of γ, the stored energy is given by

$$S_i = \alpha\frac{\gamma}{2r} \tag{9}$$

where α is a geometric constant equal to 3.

For the simulations conducted in this study the dislocation density is evaluated with the help of the first method as described by Eqs. (7) and (8). In order to normalize the values provided by this approach a new factor is introduced in order to obtain a reference value for the maximum occurring dislocation density. This value can be determined with the help of the tensile stress according to the equation

$$R_m \approx \frac{1}{2}MGb\sqrt{\rho_{max}} \tag{10}$$

where R_m is the tensile strength, M the Taylor factor, G the shear modulus, b the Burgers vector, and ρ_{max} the corresponding reference value of the dislocation density. According to this method the maximum occurring dislocation density amounts to 4.7×10^{15} m^{-2}. The so determined distribution of the stored dislocation density in the starting microstructure is given in Fig. 2.

2.7. Processing details, mesh parameters, and simulated temperature

The cellular automaton model is applied to a Ti stabilized interstitial free (IF) steel sheet. The steel slab was after continuous casting reheated at about 1500 K in a walking beam furnace and

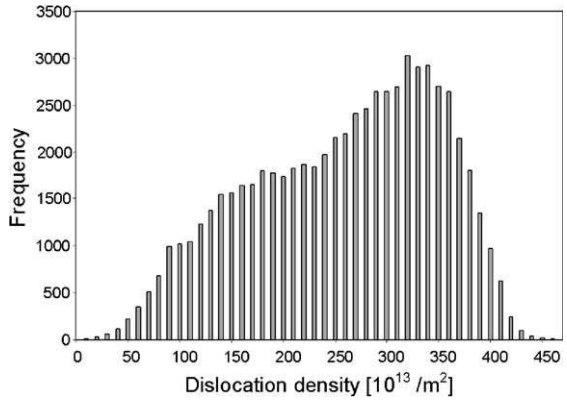

Fig. 2. Distribution of the evaluated dislocation density in the investigated area. The maximum occurring dislocation density is equal to $470 \times 10^{13}\ \mathrm{m}^{-2}$.

subsequently hot-rolled completely in the austenitic range, i.e., above the A_{r3} temperature. The subsequent transformation to ferrite during cooling results in a homogeneous, nearly random crystallographic texture through the specimen thickness. The hot band thickness prior to cold rolling was 3 mm. After hot rolling the specimen was cold rolled to an engineering strain of 75% ($\varepsilon = \Delta d/d_0$, where Δd is the thickness reduction and d_0 the starting thickness). The heat treatment simulations were conducted under the assumption of isothermal conditions at a temperature of 1000 K. The cell size of the cellular automaton, λ_m, was chosen as 0.1 μm according to the step size of the underlying EBSD measurements.

2.8. Characterization of the starting microstructure (as cold-rolled)

EBSD measurements were carried out on the as cold rolled sample in longitudinal sections (Fig. 3). The cold rolling texture exhibits a strong α-fiber (texture components with a common crystallographic ⟨1 1 0⟩ axis parallel to the rolling direction) and a relatively weak γ-fiber (texture components with a common crystallographic ⟨1 1 1⟩ axis parallel to the sheet normal) [2,6,9]. In the cold rolled specimen used for the current simulations (Fig. 3) about 45% of the investigated area consists of α-fiber orientations (yellow), whereas only 25% can be assigned to the γ-fiber (green).

The maps reveal three different types of microstructure. Inside the α-fiber grains only a few subgrain boundaries appear, i.e., misorientations between neighboring EBSD points (point-to-point) are always below 2°, but the total accumulated orientation difference may continuously increase up to 7° over a distance of 5 μm (point-to-origin). In the γ-fiber areas, subgrain structures can be seen which are confined by low angle grain boundaries with misorientations between 2° and 15°.

In the γ-fiber grains a large frequency of subgrains with an average diameter of 1 μm is visible. These are in part surrounded by high angle grain boundaries. The dislocation density distribution as determined by using Eqs. (7) and (8) is clearly different for the two texture fibers. Deformation bands and γ-fiber areas are characterized by a high dislocation density. On the contrary, the α-fiber oriented regions reveal a smaller dislocation density. The measured area used for the simulations had a size of 40 μm × 13.6 μm (Fig. 4).

3. Simulation results and discussion

3.1. Simulation of primary recrystallization without Zener effect using different nucleation criteria

In order to identify reference microstructures for the simulations with particles we first conducted some calculations without including particle drag. The characteristic time step for these simulations, Δt, amounts to 0.54 s and the grid attack frequency, $\nu_0^{\min}$, to 1.85 s. The chosen sample area is mapped by using 400×136 automaton cells. Figs. 5–7 show simulated microstructures for three different site-saturated nucleation criteria (no particle pinning), Table 1.

The orientation map on the left-hand side of Figs. 5–7 is coded as orientation difference between the local orientation and the cube orientation ($\varphi_1 = 0°$, $\Phi = 0°$, $\varphi_2 = 0°$). The maps on the right-hand side show the stored dislocation density. Highest dislocation densities are colored in red. Blue regions have the lowest stored dislocation densities. The gray areas are recrystallized, i.e., they do not carry any further driving force.

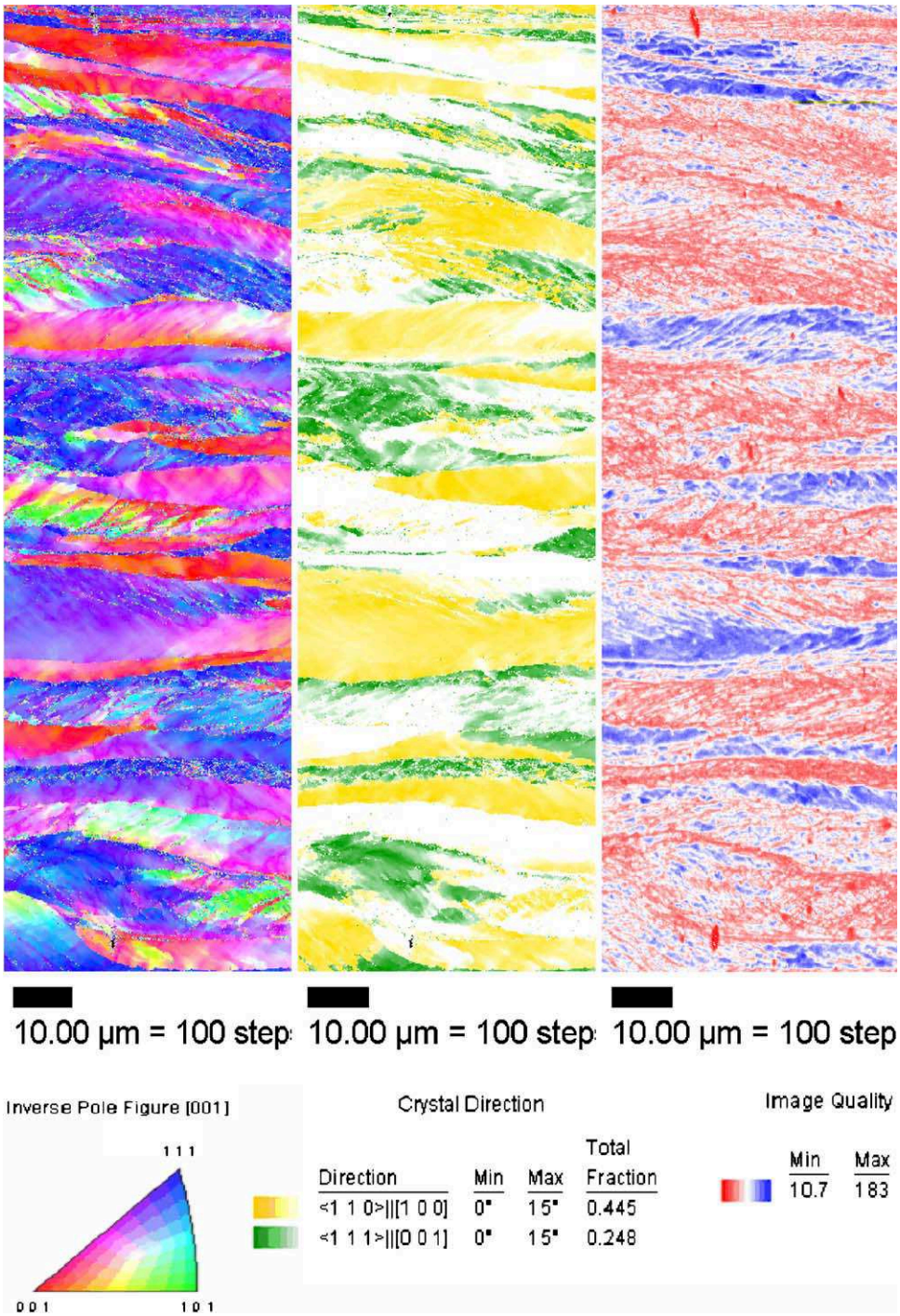

Fig. 3. EBSD measurements of a cold rolled IF steel sample: (a) inverse pole figure map with reference to the normal direction, (b) orientations close to the α-fiber (yellow) and to the γ-fiber (green) (including orientations with a maximum deviation of 15°), (c) image quality map which serves as a measure for the stored dislocation density (red = high, blue = low).

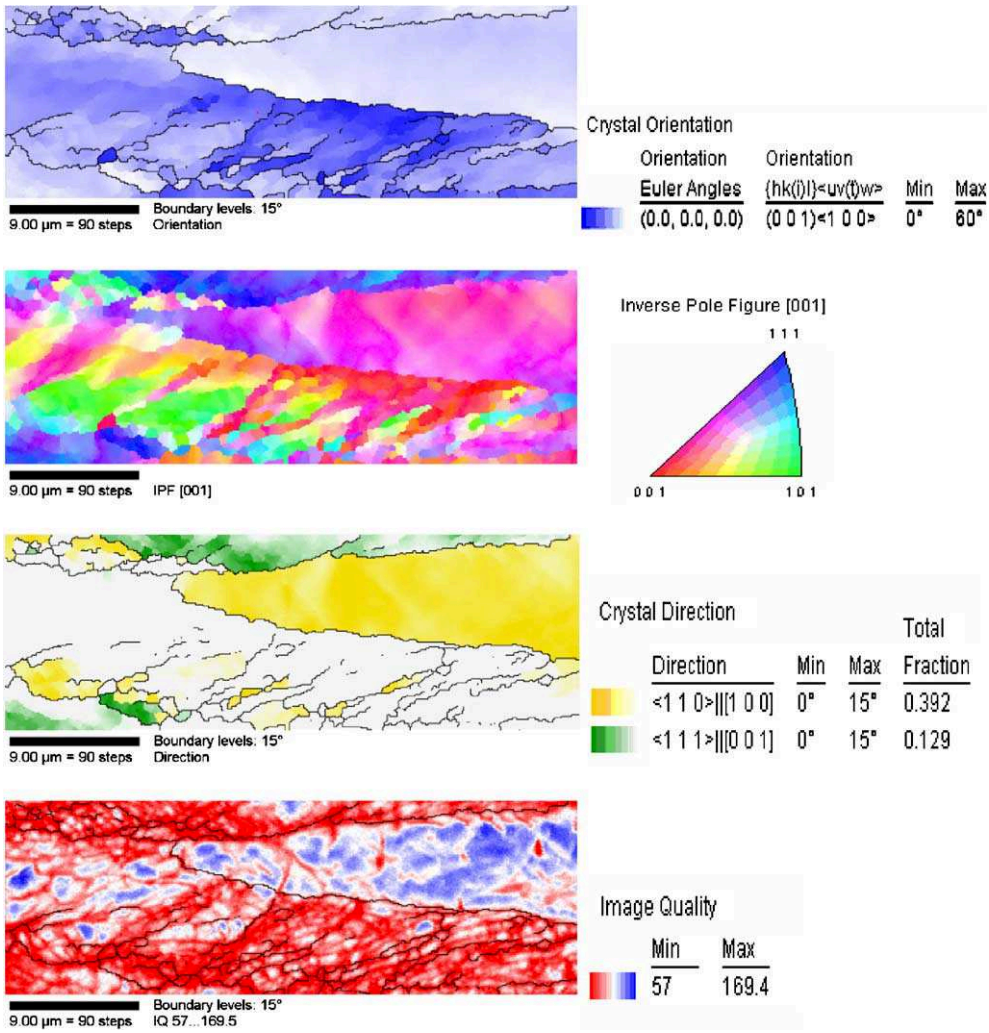

Fig. 4. EBSD measurements of the selected sample area: (a) crystal orientation using the cube orientation as a reference orientation, (b) inverse pole figure map in reference to the sheet normal direction, (c) α-fiber (yellow) and γ-fiber (green), (d) image quality as measure of the dislocation density (red = high, blue = low) according to Eqs. (7) and (8) (high angle grain boundaries are marked with thin black lines).

The black lines in both types of maps indicate large angle grain boundaries with misorientations above 15°.

The different maps, especially for nucleation criterion A (Table 1, Fig. 5), reveal that nucleation is particularly localized inside the deformation bands which are areas with high accumulated local dislocation densities. These highly deformed areas recrystallize with a grain size of about 1–2 μm. Less deformed areas exhibit a very small density of nuclei and are the last regions to be completely swept by recrystallization. Results obtained for nucleation criterion B also reveal strong nucleation clusters in areas with high dislocation densities (Table 1, Fig. 6). The average recrystallized grain size inside these clusters is between 2 and 3 μm. Cluster phenomena tend to disappear for higher threshold values, as shown exemplarily for nucleation criterion C, Table 1 (Fig. 7).

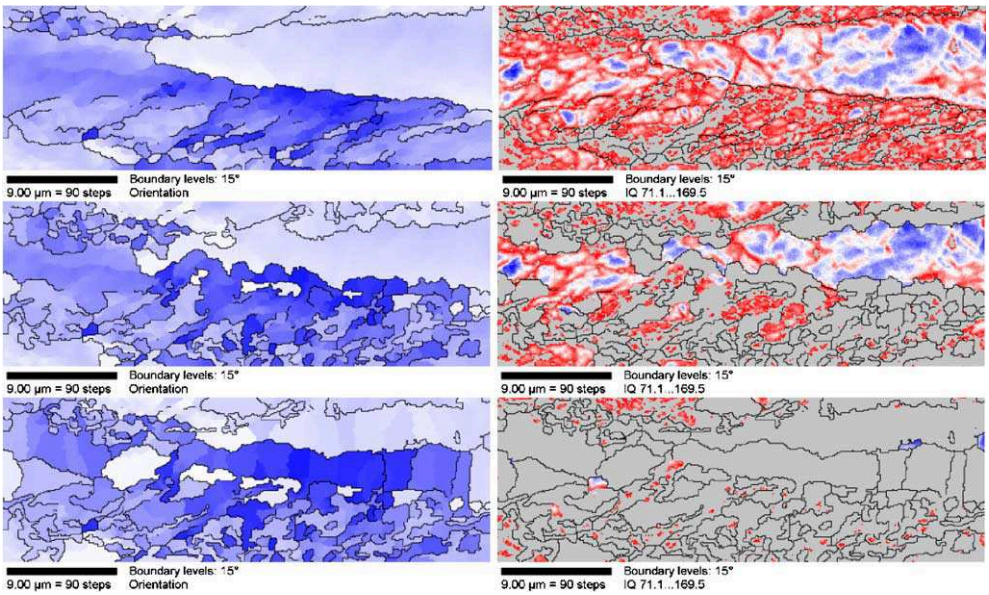

Fig. 5. Simulation results obtained for nucleation model A without particle drag (see Table 1). Recrystallization microstructures after 30, 65 and 99 vol.%. Left-hand side: crystal orientation using the cube orientation as reference. Right-hand side: dislocation density (red = high, blue = low) (high angle grain boundaries are marked with thin black lines); see color codes in Fig. 4.

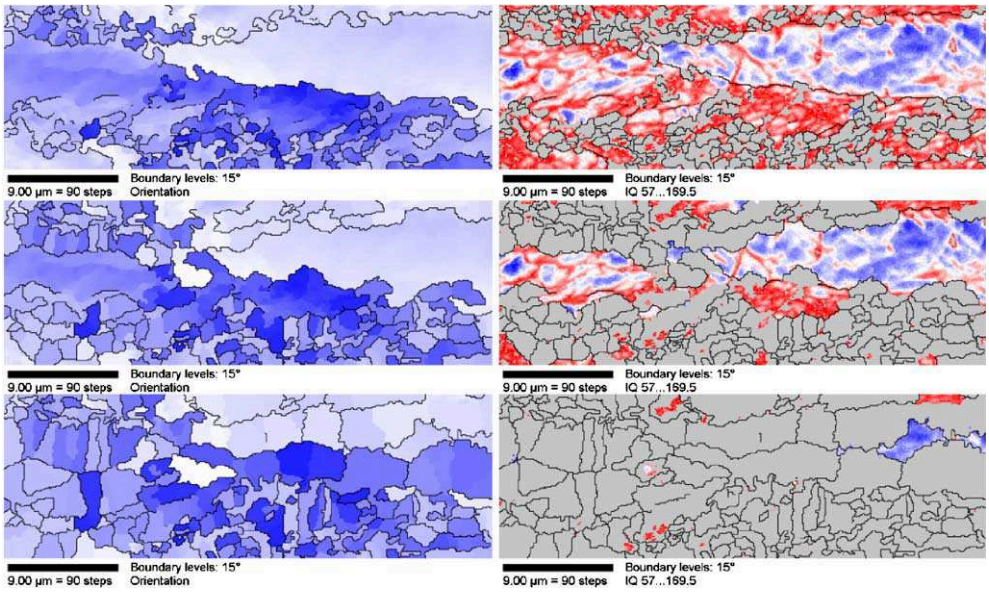

Fig. 6. Simulation results obtained for nucleation model B without particle drag (see Table 1). Recrystallization microstructures at 30, 65 and 99 vol.%. Left-hand side: crystal orientation using the cube orientation as reference. Right-hand side: dislocation density (red = high, blue = low) (high angle grain boundaries are marked with thin black lines); see color codes in Fig. 4.

It is an important topological result of these simulations that two kinds of nuclei can be observed. As prescribed by the model, nucleation takes place in areas with a large stored dislocation

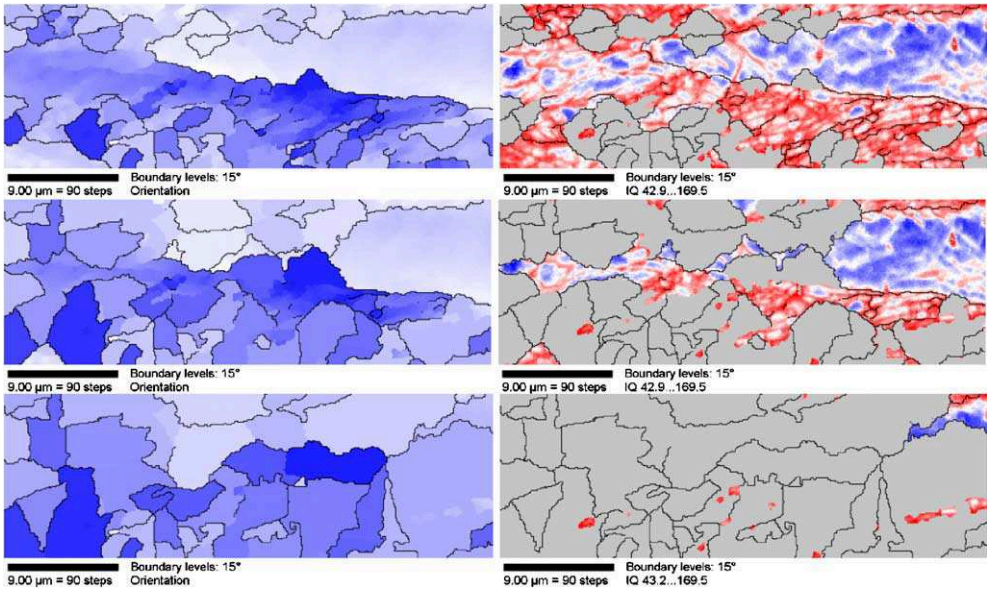

Fig. 7. Simulation results obtained for nucleation model C without particle drag (see Table 1). Recrystallization microstructures at 30, 65 and 99 vol.%. Left-hand side: crystal orientation using the cube orientation as reference. Right-hand side: dislocation density (red = high, blue = low) (high angle grain boundaries are marked with thin black lines); see color codes in Fig. 4.

Table 1
Conditions for spontaneous nucleation

Nucleation model	Nucleation criterion	Recrystallized volume fraction at $t = 0$ s
A (Fig. 5)	Cells with a dislocation density above 70% of the occurring maximum value undergo spontaneous recrystallization at $t = 0$ s (critical value: 329×10^{13} m^{-2})	~30% (16,451 cells)
B (Fig. 6)	Cells with a dislocation density above 80% of the occurring maximum value undergo spontaneous recrystallization at $t = 0$ s (critical value: 376×10^{13} m^{-2})	~10% (5272 cells)
C (Fig. 7)	Cells with a dislocation density above 90% of the occurring maximum value undergo spontaneous recrystallization at $t = 0$ s (critical value: 423×10^{13} m^{-2})	~0.5% (256 cells)

density above some critical threshold value. This means that the mechanical instability criterion which is a prerequisite for successful nucleation is automatically fulfilled for the spontaneously transformed cells, except for those which are themselves entirely surrounded by nuclei. Such cases represent trivial solutions of nucleation clustering. It occurs if a certain number of neighboring cells all fulfill independently at $t = 0$ s the condition of a critical dislocation density for nucleation (see values in Table 1).

However, according to the kinetic instability criterion which is included in the model in the form of the scaled mobility equation, spontaneously generated nuclei cannot grow if their grain boundary to the neighboring cell does not have sufficient mobility. Hence, the nuclei which are artificially formed at $t = 0$ s in the form of *potential nuclei* as described in Table 1 can only be considered as successful nuclei when the neighbor conditions described are met.

Numerous examples of such *potential nuclei* can be found inside less deformed areas, whereas the highest density of *successful nuclei,* which can freely expand after their spontaneous formation at the incipient stage of the simulation, are located

inside or close to in-grain deformation bands or in the vicinity of former grain boundaries. It is important to note that most *potential nuclei* which are formed at the beginning of recrystallization turn out to be also *successful* nuclei. This means that their neighbor cells are first, typically not themselves recrystallized (hence, sufficient local gradients in the dislocation density occur between neighbor cells) and second, that they form highly mobile large angle grain boundaries with their neighbor cells.

Another important observation is that the simulated specimen undergoes only partial recrystallization to about 99 vol.%. The corresponding mappings (Figs. 5–7) reveal two types of areas which remain unrecrystallized. The first type is indicated by the blue residual areas (indicating a small value of the stored dislocation density). These areas are mostly surrounded by large angle grain boundaries. This means that they could in principle be swept by expanding neighbor grains, but the driving forces are obviously so small that further progress of recrystallization is very slow compared to the characteristic grid attack frequency. This phenomenon can be referred to as thermodynamic decrease of the recrystallization tendency.

The second even more interesting type of unrecrystallized areas are some small red microstructure *islands* which have a sufficiently high driving force but which are surrounded by grain boundaries with a very small mobility. This phenomenon can be referred to as kinetic decrease of the recrystallization tendency. It is also referred to as *orientation pinning*. The red islands seems to be preferentially located in the deformation bands.

The kinetics of the recrystallization simulation can for the three simulations be analyzed in terms of the Avrami–Johnson–Mehl–Kolmogorov equation (JMAK) for statistical isotropic expansion of spheres,

$$X = 1 - \exp\left(-\left(\frac{t}{t_R}\right)^n\right) \tag{11}$$

where X is the recrystallized volume or area fraction, t the time, t_R the recrystallization (reference) time and n the Avrami coefficient. Site saturated 2D simulations of primary recrystallization have an Avrami coefficient equal to 2. Fig. 8 shows the results obtained from such kinetic analysis for the three different simulations. All show a substantial deviation from the typical JMAK-type growth kinetics. All curves exhibit a flattened shape when compared with the analytical equation. Also, all three simulations show Avrami coefficients below the theoretical 2D JMAK value of 2. The lower the dislocation density threshold value for nucleation is (Table 1), the larger is the deviation from the JMAK solution.

Several reasons are conceivable to explain this deviation: Firstly, nucleation is not homogeneous in the present case, but it is concentrated in areas with a large stored dislocation density. This means that the new nuclei impinge upon each other and compete at a very early stage of recrystallization unlike than in the JMAK model which makes a homogeneous assumption about the spatial

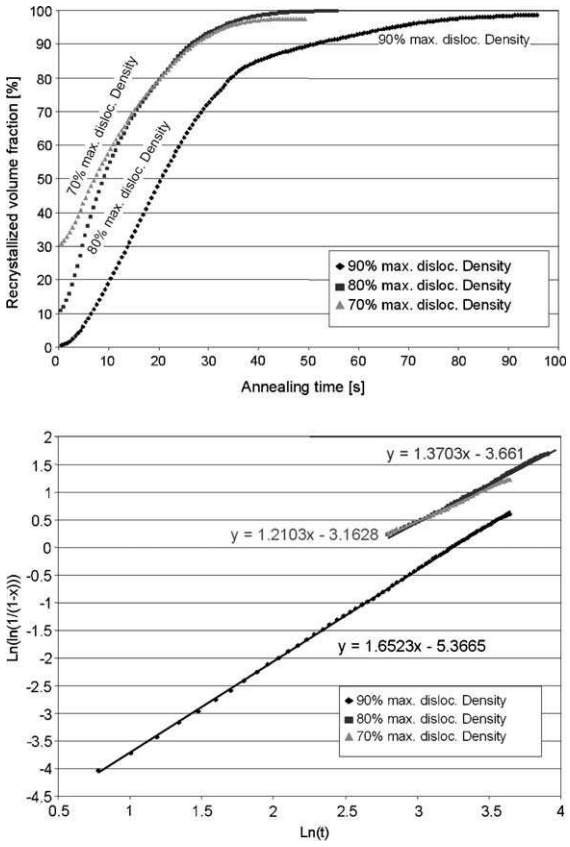

Fig. 8. Kinetics and Avrami coefficients of the recrystallization simulations shown in Figs. 5–7.

distribution of the nucleation sites. When the threshold value (dislocation density above which spontaneous nucleation occurs) becomes higher, nucleation clustering effects become more attenuated and recrystallization tends to follow the JMAK model. Secondly, the JMAK theory does not consider a heterogeneous distribution of the driving force and of the grain boundary mobility. The heterogeneous spectrum of these quantities as encountered in the starting configuration of the cellular automaton model will, on average, slow down the kinetics of recrystallization when compared to the JMAK owing to correlation effects. Finally, the discrete (cell) structure of the automaton algorithm also plays a role for the observed deviation. While the analytical model assumes a vanishing volume for freshly generated nuclei, the cellular automaton must assign at least one cell to each new nucleus. The predicted recrystallization time (around 50–100 s) is in good accord with the experimental values.

3.2. Simulation results of primary recrystallization considering Zener effects

The following simulations have been conducted using nucleation criterion B (80% of the maximum occurring dislocation density as a threshold value, see Table 1). Two models have been used for the implementation of particle pinning, namely, the classical Zener description, $p_r = -1.5\gamma f/r$ and a modified Zener model, $p_r = -2.6\gamma f^{0.92}/r$ (see details in Section 2). Since the particle radius is used as a constant (500 Å), simulations have been carried out with different magnitudes of the particle volume fraction.

The first step of the simulation study is to determine for which minimum value of the volume–particle radius ratio (*f*/*r* ratio) the recrystallization is stopped by the presence of particles. This ratio is identified by conducting an Avrami analysis for all simulations for different volume–radius ratios between 0 and 8 μm^{-1} (Fig. 9). Fig. 10 shows some selected simulated microstructures for different particle volume fractions.

According to the values of the *f*/*r* ratio, three different recrystallization regimes can be observed. The first regime can be identified for values below

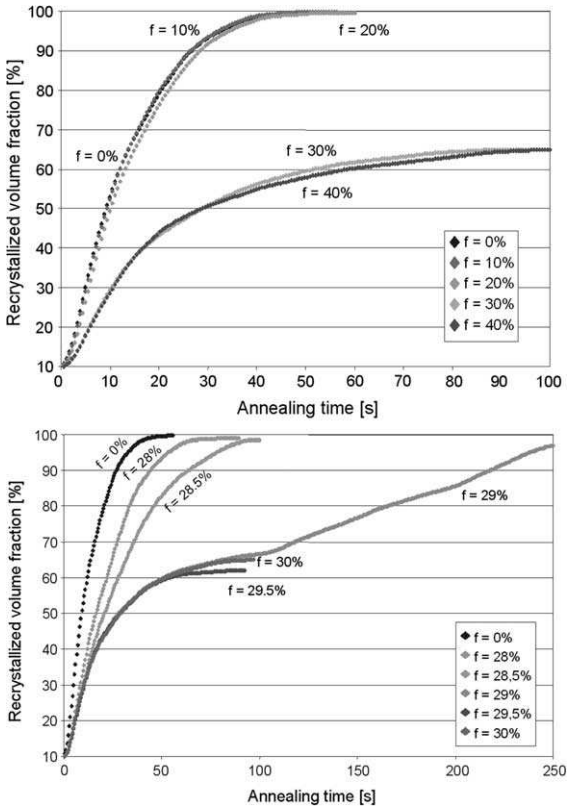

Fig. 9. Kinetics of recrystallization simulations with different particle volume fractions; classical Zener pinning assumed on the inherited grain boundaries.

5.7 μm^{-1}. In this range the sample recrystallizes completely. This means that the pinning forces exerted by the particles residing on the inherited grain boundaries are overcome by the local driving forces. When compared with the corresponding recrystallization simulations which were conducted without particle drag effects, the recrystallization observed in the current case is retarded but it is not suppressed.

The second regime can be identified for values larger than 5.9 μm^{-1}. In this case the primary recrystallization stops after sweeping about 65% of the sample volume. The final microstructure reveals a number of unrecrystallized regions.

The third regime can be identified for intermediate values between 5.7 and 5.9 μm^{-1}. In this range the recrystallization exhibits a transition regime. The occurrence of such a behavior is due to the

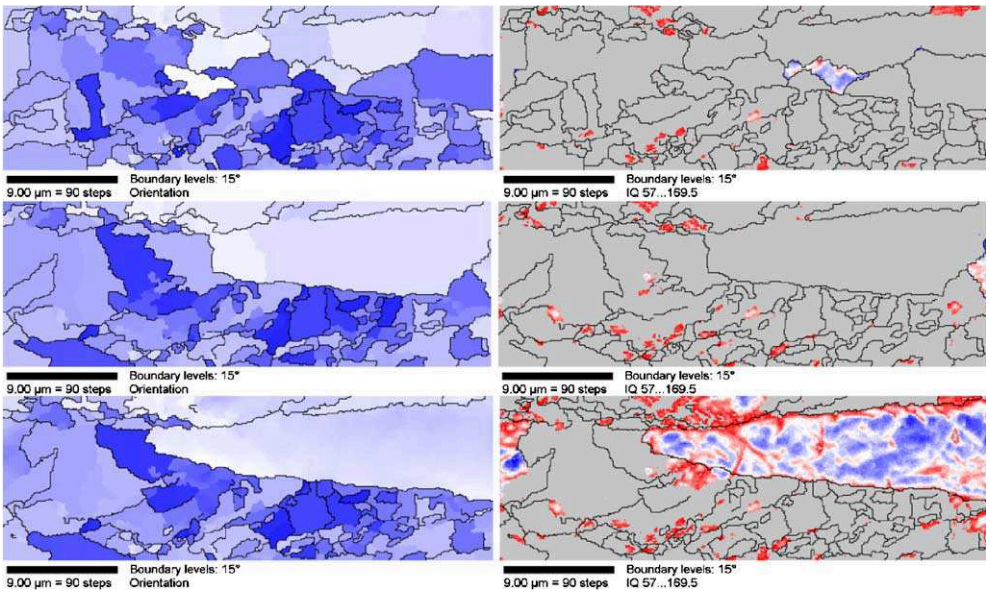

Fig. 10. Set of final simulated microstructures for different values of the precipitated volume fractions, f, of 28%, 29% and 30% (from top to bottom). The nucleation criterion was that all cells with a dislocation density above 80% of the occurring maximum value undergo spontaneous recrystallization at $t = 0$ s ($>376 \times 10^{13}$ m^{-2}) (see criterion B in Table 1); classical Zener pinning.

fact that most portions of the recrystallization front are successfully pinned by the particles. However, locally the particle pinning forces are overcome so that recrystallization expands rapidly further in those areas. This transition or two-stage recrystallization behavior could be termed *percolation recrystallization* regime. In such cases those local sites, where single grains can overcome the pinning force, assume the role of a nucleus which percolates across grain boundaries if the pinning forces are weak or the local driving force is very high. Since only a few such sites occur, the final grain sizes can become quite large in such cases. The transition regime occurs within a relatively sharp interval of the *f/r* values. This means that the driving forces occurring locally at the recrystallization front encounter particles which, on average, impose a drag force of almost the same magnitude. This average magnitude amounts to about 7 MPa for the present case, i.e., particle pinning forces must exceed this average value in order to completely suppress primary static recrystallization everywhere in the system.

Fig. 11 shows the evolution of the α- and γ-texture fibers during the simulated annealing treatment for different *f/r* ratios. The α-fiber is a typical cold rolling fiber for IF steels. It collects texture components with a common crystallographic ⟨1 1 0⟩ axis parallel to the rolling direction. The γ-fiber is a typical annealing fiber. It presents texture components with a common crystallographic ⟨1 1 1⟩ axis parallel to the sheet normal) [2,3].

The data show that for *f/r* ratios below 5.7 μm^{-1} the evolution of both, α-fiber and γ-fiber, is in good accord with the texture evolution typically observed for low-carbon steels, i.e., the γ-fiber increases and the components on the α-fiber decrease. A special feature of these simulations is the relatively late increase of the γ-fiber. Until a recrystallized volume fraction of 50% is reached, the γ-fiber orientations remain approximately constant at about 13 vol.%. After that it drops rapidly as a function of time.

For *f/r* ratios between 5.7 and 5.9 μm^{-1} the evolution of the α- and γ-fiber texture components is reversed at the beginning of recrystallization. With an increasing progress of recrystallization, however, the γ-fiber orientations become quite strong corresponding to a pronounced drop of the orientations on the α-fiber.

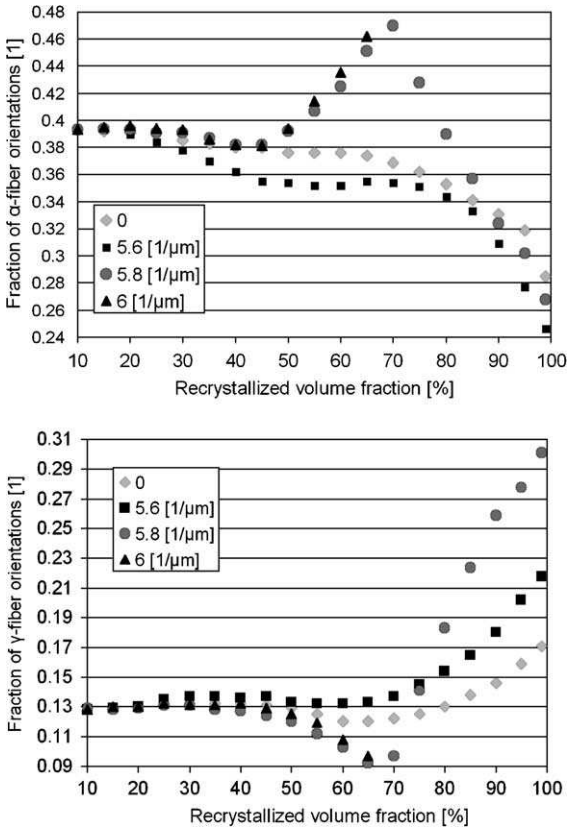

Fig. 11. Evolution of the α- and γ-fiber orientations during the simulated annealing under consideration of particle drag for different ratios of the volume fraction and particle radius, *f*/*r*.

For *f*/*r* ratios larger than 5.9 μm^{-1} the same reversed trend as found between 5.7 and 5.9 μm^{-1} is observed. However, no increase in the γ-fiber occurs before the recrystallization ceases to proceed. Consequently, after a recrystallized volume fraction of 50% the α-fiber still dominates the texture.

The results obtained for the predictions which were conducted by using the Zener–Friedel instead of the classical Zener model are very similar to the data shown above. When using the same starting configurations as for the Zener calculations, especially the same assumed particle radius of 0.05 μm, the transition regime occurs for a particle volume fraction between 14% and 15%. This is consistent with the analytical result for the critical volume fraction associated with the Friedel–Zener pinning force, f_{FZ}.

$$\frac{3}{2}\gamma\frac{f_Z}{r} = 2.6\gamma\frac{f_{FZ}^{0.92}}{r} \Longleftrightarrow f_{FZ} = \exp\left(\frac{\ln(0.58 f_Z)}{0.92}\right), \quad \text{i.e., } f_{FZ} \approx 0.141 \tag{12}$$

4. Conclusions

We used a cellular automaton model for the simulation of the recrystallization texture of an 80% cold rolled interstitial free (IF) steel with and without consideration of particles on the inherited grain boundaries. The model was applied to experimentally obtained high resolution EBSD data. Depending on the ratio of the precipitated volume fraction and the average radius of the particles, *f*/*r*, the simulations revealed three different regimes for the influence of particle pinning on the resulting microstructures, kinetics and textures. The first regime which occurred for small values of the *f*/*r* ratio on the former grain boundaries was characterized by complete, though retarded recrystallization. The second regime which occurred for intermediate values of the *f*/*r* ratio on the former grain boundaries was characterized by a partially suppressed progress of recrystallization. The third regime which occurred for large values of the *f*/*r* ratio on the former grain boundaries was characterized by a kinetic transition, i.e., most of the recrystallization front was successfully pinned by particles except for some small areas where recrystallization could percolate into neighboring grains. This regime, therefore, revealed a two-stage recrystallization behavior which was be referred to as percolation recrystallization.

References

[1] W.B. Hutchinson, Int. Mat. Rev. 29 (1984) 25.
[2] M. Hölscher, D. Raabe, K. Lücke, Steel Res. 62 (1991) 567.
[3] D. Raabe, K. Lücke, Scripta Metall. 27 (1992) 1533.
[4] C. Klinkenberg, D. Raabe, K. Lücke, Steel Res. 63 (1992) 227.
[5] D. Raabe, C. Klinkenberg, K. Lücke, Steel Res. 64 (1993) 262.
[6] P. Juntunen, D. Raabe, P. Karjalainen, T. Kopio, G. Bolle, Metall. Mater. Trans. A 32 (2001) 1989.

[7] D. Raabe, K. Lücke, Mater. Sci. Technol. 9 (1993) 302.
[8] D. Raabe, P. Klose, B. Engl, K.-P. Imlau, F. Friedel, F. Roters, Adv. Eng. Mater. 4 (2002) 169.
[9] I. Thomas, S. Zaefferer, F. Friedel, D. Raabe, Adv. Eng. Mater. 5 (2003) 566.
[10] D. Raabe, Phil. Mag. A 79 (1999) 2339.
[11] C. Zener, Private communication to C.S. Smith. Cited in Trans. Am. Inst. Min. Engrs 175 (1948) 15.
[12] D. Raabe, Steel Res. 66 (1995) 222.
[13] J. von Neumann, in: W. Aspray, A. Burks (Eds.), Papers of John Von Neumann on Computing and Computer Theory, Charles Babbage Institute Reprint Series for the History of Computing, vol. 12, MIT Press, Cambridge, MA, 1987.
[14] S. Wolfram, Theory and Applications of Cellular AutomataAdvanced Series on Complex Systems, selected papers 1983–1986, vol. 1, World Scientific, Singapore, 1986.
[15] D. Raabe, Computational Materials Science, Wiley-VCH, Weinheim, 1998.
[16] D. Raabe, Ann. Rev. Mater. Res. 32 (2002) 53.
[17] D. Raabe, F. Roters, F. Barlat, L.-Q. Chen (Eds.), Continuum Scale Simulation of Engineering Materials, WILEY-VCH, Weinheim, 2004.
[18] H.W. Hesselbarth, I.R. Göbel, Acta Metall. 39 (1991) 2135.
[19] C.E. Pezzee, D.C. Dunand, Acta Metall. 42 (1994) 1509.
[20] R.K. Sheldon, D.C. Dunand, Acta Mater. 44 (1996) 4571.
[21] C.H.J. Davies, Scripta Metall. Mater. 33 (1995) 1139.
[22] V. Marx, D. Raabe, O. Engler, G. Gottstein, Text. Microstruct. 28 (1997) 211.
[23] V. Marx, F.R. Reher, G. Gottstein, Acta Mater. 47 (1998) 1219.
[24] C.H.J. Davies, Scripta Mater. 36 (1997) 35.
[25] C.H.J. Davies, L. Hong, Scripta Mater. 40 (1999) 1145.
[26] D. Raabe, R. Becker, Model. Simul. Mater. Sci. Eng. 8 (2000) 445.
[27] D. Raabe, Comput. Mater. Sci. 19 (2000) 13.
[28] D. Raabe, F. Roters, V. Marx, Text. Microstruct. 26–27 (1996) 611.
[29] K.G.F. Janssens, Model. Simul. Mater. Sci. Eng. 11 (2003) 157.
[30] D. Raabe, Acta Mater. 52 (2004) 2653.
[31] F.J. Humphreys, M. Hatherly, Recrystallization and Related Annealing Phenomena, Pergamon, New York, 1995.
[32] R.D. Doherty, K. Li, K. Kershyup, A.D. Rollet, M.P. Anderson, in: J.B. Bilde-Sorensen et al. (Eds.), Materials Architecture, 10th Risø Symposium, Risø National Laboratory, Roskilde, Denmark, 1989, p. 31.
[33] R.D. Doherty, D.J. Srolovitz, A.D. Rollet, M.P. Anderson, Scripta Metal. 21 (1987) 675.
[34] E. Nes, E. Ryum, O. Hunderi, Acta Metall. 33 (1985) 11.
[35] O. Hunderi, E. Nes, N. Ryum, Acta Metall. 37 (1989) 129.
[36] N. Louat, Acta Metall. 30 (1982) 1291.
[37] M. Furtkamp, G. Gottstein, D.A. Molodov, V.N. Semenov, L.S. Shvindlerman, Acta Mater. 46 (1998) 4103.
[38] Y. Avramov, A. Gvozdev, Phys. Met. 36 (1973) 198.
[39] G. Gottstein, L.S. Shvindlerman, Grain Boundary Migration in Metals—Thermodynamics, Kinetics, Applications, CRC Press, Boca Raton, 1999.
[40] S.-H. Choi, Acta. Mater. 51 (2003) 1775.
[41] S.-H. Choi, Y.-S. Jin, Mater. Sci. Eng., A 371 (2004) 149.
[42] D. Raabe, M. Sachtleber, Z. Zhao, F. Roters, S. Zaefferer, Acta Mater. 49 (2001) 3433.